Stability of gas channels in a dense suspension in the presence of obstacles

Raphaël Poryles,[1] Germán Varas,[2] and Valérie Vidal[1]
[1]*Laboratoire de Physique, École Normale Supérieure de Lyon, Université de Lyon–CNRS, 46 Allée d'Italie, 69364 Lyon Cedex 7, France*
[2]*Instituto de Física, Pontificia Universidad Católica de Valparaíso, Av. Universidad 330, Valparaíso, Chile*
(Received 12 December 2016; revised manuscript received 4 May 2017; published 23 June 2017)

We investigate experimentally the influence of a fixed obstacle on gas rising in a dense suspension. Air is injected at a constant flow rate by a single nozzle at the bottom center of a Hele-Shaw cell. Without obstacles, previous works have shown that a fluidized zone is formed with a parabolic shape, with a central air channel and two granular convection rolls on its sides. Here, we quantify the influence of the obstacle's shape, size, and height on the location and dynamics of the central air channel. Different regimes are reported: the air channel can simply deviate (stable), or it can switch sides over time (unstable), leading to two signatures not only above the obstacle, but sometimes also below it. This feedback also influences the channel deviation when bypassing the obstacle. A wake of less or no motion is reported above the largest obstacles as well as the maximum probability of gas location, which can be interesting for practical applications. The existence of a critical height $h_c \simeq 7$ cm is discussed and compared with the existence of an air finger that develops from the injection nozzle and is stable in time. A dimensionless number describing the transition between air fingering and fracturing makes it possible to predict the channel's stability.

DOI: 10.1103/PhysRevE.95.062905

I. INTRODUCTION

Soil failure is one of the most significant natural hazards that can threaten human activities. As a consequence, its response to an externally applied mechanical stress such as loading or seismic waves has been widely investigated [1,2]. Many of these studies propose an alternative approach to classical solid rupture by considering that, above a critical stress, the ground behaves like a frictional fluid rather than yielding like a solid [3]. The cohesive forces between rocks and soil particles are not strong enough to prevent internal structure movement, and the soil can be viewed as a granular medium undergoing a so-called *fluidization*. This latter can be simply defined as a process whereby a granular material goes from a static, solidlike behavior to a dynamic, fluidlike state, also called a *dense suspension*.

Fluidization processes are numerous in natural or human-made three-phase flows, where the constraint corresponds to gas invasion in a liquid-saturated ground or granular medium. In geophysics, the generation of pockmarcks [4,5] or mud volcanoes [6–8] are among many other examples. Man-made applications include, on the one hand, air sparging. This technique of soil remediation consists in injecting high-pressure gas into the ground to remove the water contamination by volatile compounds [9–11]. On the other hand, three-phase flows are of drastic importance in multiphase catalytic reactors, where gas is injected in a mobile, immersed porous medium to enhance chemical reactions [12,13].

To understand and quantify this fluidization process, fundamental studies have been performed at the laboratory scale, in which gas invades, through a single injection point, a liquid-saturated granular medium. In the particular case of buoyancy-driven systems, it has been found that after an initial invasion regime where the gas either percolates or fractures through the granular bed, a fluidized zone of parabolic shape is formed [9,11,14–20]. In the stationary regime, the gas mainly rises through a central channel at the vertical of the injection point. Bubbles are created in this channel and rise by buoyancy, entraining the surrounding solid particles. Two granular convection rolls thus form on both sides of the central gas channel, which entrain the grains and are responsible for the observed parabolic shape [17,19,21].

These experiments usually model the ground particles as spherical grains, with a peaked distribution around an average particle diameter. Real soils, however, are often characterized by large heterogeneities such as solid rocks, which can prevent the ground motion [1,14]. Granular flows around obstacles have been investigated in the dry case, showing the formation of a dead zone corresponding to the grains-obstacle interaction [22,23]. However, to our knowledge, no systematic study of the influence of obstacles on gas rising in a dense suspension has been performed.

In this work, we investigate the influence of fixed obstacles of different shape, size, and location on the dynamics of gas channels rising through a dense suspension. We focus on the simplest case of a single obstacle, fixed in the laboratory frame, and we analyze the stability of the central gas channel when passing this obstacle, as well as the location of maximum gas concentration in the system. The results, which may be interesting for practical application such as ground remediation or heterogeneous catalysis, are compared to the case of homogeneous suspensions, i.e., without obstacle.

II. EXPERIMENTAL SETUP

The experimental setup consists of a vertical Hele-Shaw cell made of two glass plates (40×30 cm) separated by a gap $e = 2$ mm. The cell is filled with particles immersed in water in which a single obstacle of a different shape and size is located at height h [see Table I and Fig. 1(a)]. The obstacles are magnets (HKCM Engineering e.K.) whose thickness equals the cell gap e so that no grains, liquid, or air can be trapped or flow on its faces. They are fixed by means of a second, more powerful magnet (a cylinder of diameter 5 mm and height 28 mm, HKCM Engineering e.K.) located outside

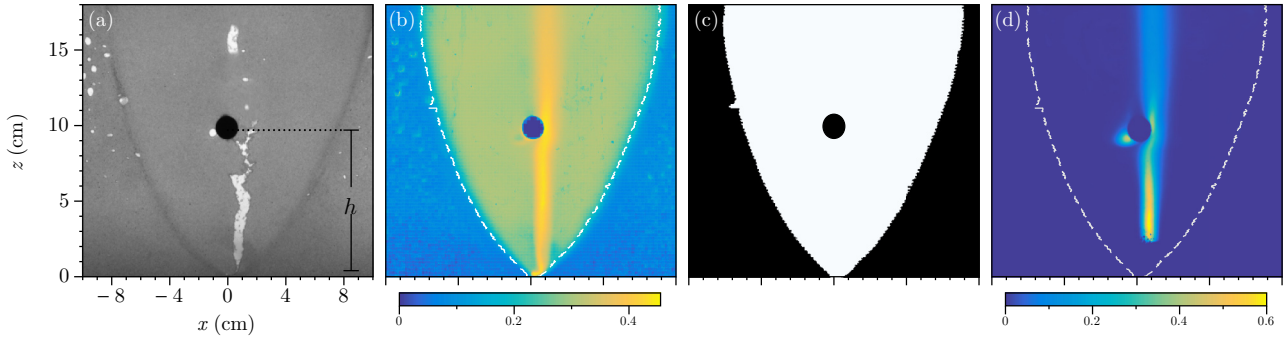

FIG. 1. Experimental setup and image processing (circular obstacle, $D = 1.5$ cm, $h = 10$ cm). (a) Example of experimental snapshot. We can distinguish the obstacle (black circle at height h), the air rising through the granular bed, bubbles trapped in the upper part, and the central fluidized zone, marked by a slightly darker contour. (b) Cumulated motion M computed with Eq. 1 (threshold 1%). The color bar indicates the probability of motion in the system over the total experiment duration. The white dashed line is the contour of the fluidized zone determined after binarization of the cumulated motion M (threshold 20%). (c) Binarized image representing the fluidized zone (in white) and the area without motion (in black). The contour of the fluidized zone is extracted from this image (see the text). (d) Cumulative image C computed from Eq. (2). The color bar represents the probability of the presence of bubbles in the system.

the glass plates. This magnet also ensures that the obstacle does not move during the entire experiment. To study the effect of the obstacle shape, three magnet geometries are used (Table I): circular obstacles of diameter $D = [1,1.5,4]$ cm; square obstacles of side $D = [1,4]$ cm, and diamond-shaped obstacles, which are simply the square obstacles rotated by 45°. In this last case, the obstacle size is considered as its typical horizontal length, and thus it includes a factor $\sqrt{2}$ with respect to the square obstacle (Table I). The obstacle height h, measured from the cell bottom to the center of the obstacle, is varied from $h = 2.5$ to 15 cm from the cell bottom, at the vertical of the air injection nozzle [Fig. 1(a)].

To ensure reproducible initial conditions, the following protocol is used. Once the obstacle is fixed in the cell, the particles are added using a funnel, up to a height $h_g = 20$ cm. They consist of polydisperse spherical glass beads (Sovitec) of typical diameter $d = 318 \pm 44$ μm. This latter, measured with a microscope (Optika B-163), displays a roughly Gaussian size distribution [17]. The cell is then entirely filled with distilled water, sealed at its top, and turned upside down so that the particles are decompacted and sediment gently. Right before the full particle sedimentation, the cell is turned back to its initial, vertical position and the grains are allowed to sediment once more. This method makes it possible to remove all the bubbles trapped initially in the granular layer. The surface is then gently leveled with a rod, and the excess of water is removed until the water layer above the granular bed is set to $h_w = 2$ cm. The initial condition is therefore an immersed, loose-packed granular bed—or a dense suspension—in which an obstacle is trapped.

TABLE I. Shape, symbol, size D, and height h of the obstacles located in the immersed granular bed.

Shape	Symbol	D (cm)	h (cm)
circle	◯	1	2.5, 5, 7.5, 10, 15
circle	◯	1.5	2.5, 5, 7.5, 10, 12.5, 15
circle	◯	4	3.5, 5, 7.5, 10
square	□	1, 4	5, 10
diamond	◇	1.4, 5.7	5, 10

At time $t = 0$, air is injected at a constant flow rate through a nozzle of inner diameter 1 mm, located at the bottom center of the cell, by means of a digital mass flow controller (M+W Instruments, model D-6311). The flow rate is fixed at $Q = 1.98$ mL/s for all experiments, high enough to ensure a quick stabilization of the central air channel, of the order of 1 min [17]. A LED panel at the back of the cell provides a homogeneous light, and the dynamics of the experiment is followed by means of a camera (PixeLINK, model PL-B741U, 1280×800 px^2) recording one image every 2 s. All experiments last for 20 h in order to capture the long-time dynamics of the system.

III. IMAGE PROCESSING

This section details the image analysis, which is aimed at separating the two mechanisms at stake in the system. First, with or without obstacles, we observe at long times the formation of a central fluidized zone of roughly parabolic contour, corresponding to slow grain motion [Fig. 1(a) and Sec. III A]. Then, the air rise tends to choose preferential pathways through the dense suspensions [Fig. 1(d)], which will be characterized in Sec. III B.

A. Fluidized zone

The central fluidized zone corresponds to the cumulation of grain motion in the system through time. To quantify this region, we define from the image sequence $\{I_k\}$ a *cumulated motion* image M given by

$$M = \frac{1}{N}\sum_{k=1}^{N-1} \mathcal{B}_{1\%}(|I_{k+1} - I_k|), \tag{1}$$

where N is the total number of frames, $|I_{k+1} - I_k|$ is the absolute value of the difference between two consecutive images, and $\mathcal{B}_{1\%}$ is a binarization function returning 1 when $|I_{k+1} - I_k| > 1\% \max(|I_{k+1} - I_k|)$, and 0 otherwise. M therefore corresponds to the fraction of time over the whole experiment for which motion was experienced in the system, with a 1% threshold.

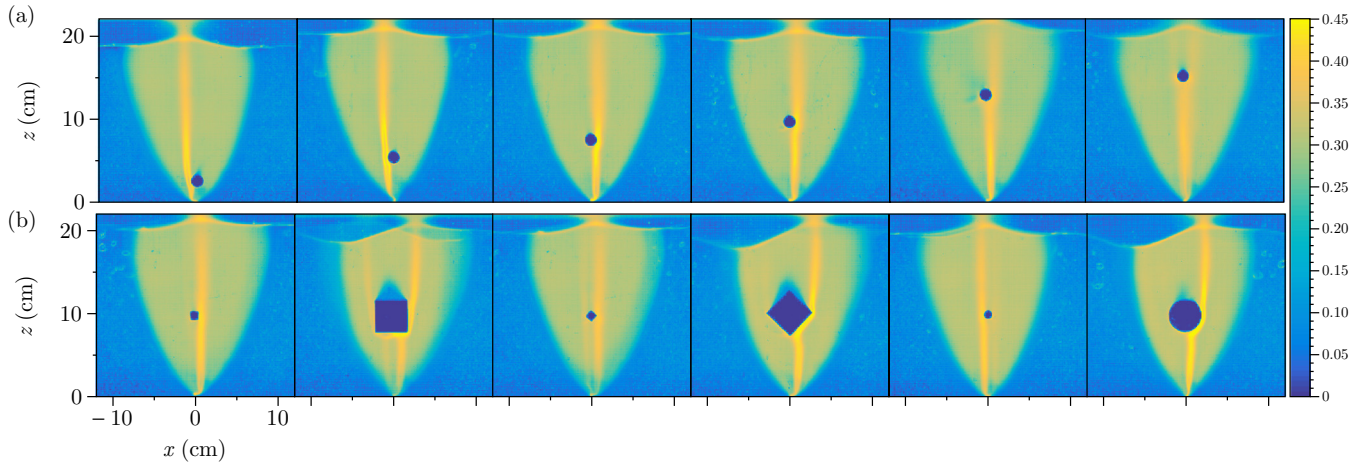

FIG. 2. Cumulated motion M for different obstacle size D and heights h [symbol, D (cm)]. (a) Circular obstacle [(◯,1.5), from left to right, $h = 2.5$, 5, 7.5, 10, 12.5, and 15 cm]. (b) Different shapes of obstacles for a fixed height [$h = 10$ cm, from left to right, (□,1); (□,4); (◇,1.4); (◇,5.7); (◯,1); (◯,4)]. The figures show the deviation of the air channel by the obstacle and the formation of a wake above large obstacles. In some cases, two channels are clearly distinguished [(b), second and third image, cf. Sec. IV].

Figure 1(b) displays the cumulated motion image M for the example of a circular obstacle ($D = 1.5$ cm, $h = 10$ cm). Three different zones are clearly distinguishable in the image: (i) the central air rise (in yellow, ∼45% motion), which concentrates the largest motion; (ii) the lateral grain motion (in green, ∼30% motion), whose contour (white dashed line) clearly delimits the boundary of the fluidized zone; and (iii) the grains outside the central moving zone (in blue, ∼0–5 % motion), which remain roughly still over all the experiment. Note that the motion outside the fluidized zone is not strictly zero here. Indeed, the cumulated motion image computation takes into account the transient regime, during which the air channel(s) can explore by percolation or fracture a space much larger than the central fluidized zone—see, for instance, the bubbles trapped on the left upper part of the image, outside the fluidized zone, in Fig. 1(a).

We quantify the fluidized zone as the region where more than 20% of the motion was observed during the whole experiment [white region, Fig. 1(c)]. The 20% threshold is chosen such that it excludes successfully the small, sporadic motions outside the central zone observed mainly at the beginning of the experiments, in the transient regime. The contour systematically matches the fluidized zone border observed in the raw images at long times [dark contour, Fig. 1(a) and white dashed lines, Fig. 1(b)].

B. Gas preferential pathways

In addition to the previous calculation, which gives information on the motion in the system, it is interesting to quantify the presence of gas bubbles in the granular bed. To do so, we estimate a *cumulated image*, C, as follows. First, each image I_k is binarized so that a value 1 is attributed to the presence of a bubble, and it is 0 otherwise. The binarized images are then stacked and normalized by the total image number, giving

$$C = \frac{1}{N}\sum_{k=1}^{N-1} \mathcal{B}_{40\%}(I_k), \qquad (2)$$

where $\mathcal{B}_{40\%}$ is a binarization function with a 40% threshold. This latter value is estimated to get the best estimation between bubbles and immersed grains in the images. C therefore represents the probability of the presence of bubbles in the system over all the experiment. An example of a cumulated image is displayed in Fig. 1(d), where it is possible to observe the central air channel, the deviation by the obstacle, the maximum probability around $z \simeq 3$ cm, and the signature of gas bubbles trapped from time to time on the left side of the obstacle [visible in Fig. 1(a)].

IV. EXPERIMENTAL RESULTS

A. Motion in the system

Figure 2 presents the cumulated motion M for different obstacle shape, size D, and height h. Different qualitative observations can be made. First, the contour of the fluidized zone (the border between the green and blue regions) does not vary drastically regardless of the size, shape, or height of the obstacle. Although it can be slightly deformed for large obstacles [see, for instance, Fig. 2(b), second, fourth, and sixth images], it always follows a roughly parabolic shape, and it is not drastically increased when the obstacle size is increased. Note that in the case of large obstacles, the average free surface displacement is mostly shifted to one side, corresponding to the side chosen preferentially by the central air channel to bypass the obstacle [Fig. 2(b), second, fourth, and sixth images].

Second, above large obstacles, a wake is clearly visible [blue zone; see, for instance, Fig. 2(b), square obstacle $D = 4$ cm]. It also exists for smaller obstacles [Fig. 2(a), first image], but it is less visible. As for the grains outside the fluidized zone, the wake corresponds to a region where the motion is nonzero, but greatly reduced with respect to the average motion in the fluidized zone. A thorough quantification of the wake size is presented in Sec. IV C.

Finally, depending on the parameters, we report different preferential pathways of the central air channel. Because the obstacle is centered on the vertical of the injection nozzle, we

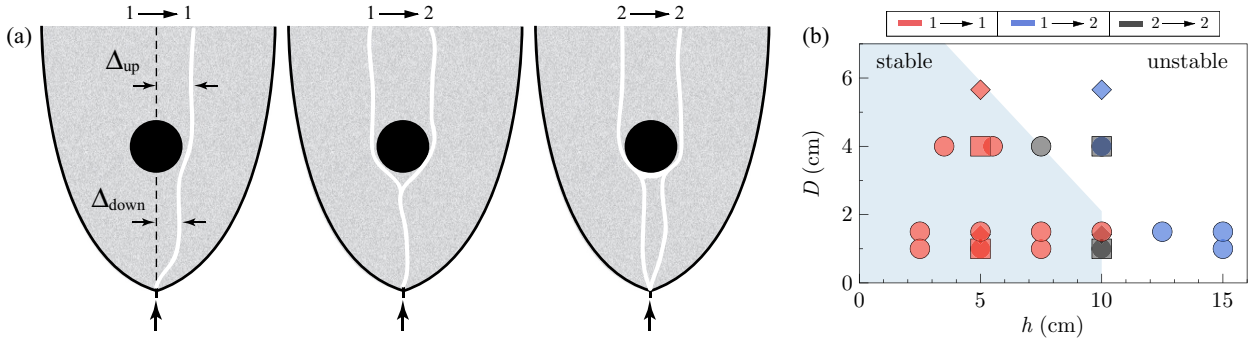

FIG. 3. (a) Sketch of the possible air pathways. The upper labels indicate the number of channel pathways before ⟶ after the obstacle, and the symbols represent the obstacle shape. To quantify the deviation of the central air channel induced by the obstacle, we define the distance between the vertical of the injection nozzle and the air channel below (Δ_{down}) and above (Δ_{up}) the obstacle. (b) Phase diagram (D,h) for the number of air channels before → after the obstacle. The symbols represent the obstacle shape. The light blue region indicates the parameters for which a single channel is observed before and after the obstacle.

expect qualitatively that the rising gas bubble or finger will choose randomly one side or the other to bypass the obstacle. However, due to the formation of preferential pathways (i.e., it is easier for the air to follow a previously opened path rather than forming a new one in the dense suspension), different regimes are observed, which are described in Sec. IV B.

B. Stability of the central gas channel

The central gas pathway, visible in Fig. 1(a), does not necessarily follow a vertical path from the injection nozzle to the obstacle. Indeed, some fluctuations can appear close to the injection point, which can deviate the channel temporarily or permanently when the air penetrates the dense suspension. These fluctuations, coupled with the fact that the air has to bypass the obstacle, give rise to three different signatures of the gas pathways over the whole experimental time [Figs. 2 and 3(a)]: (i) The gas either rises vertically or is slightly deviated on one side, and it bypasses the obstacle on this same side [case 1 → 1, Fig. 3(a), left]; in this case, the obstacle stabilizes the gas pathway both under and above the obstacle. (ii) The gas rises roughly vertically, but changes intermittently in time the side by which it bypasses the obstacle, giving on average a single path below and two signatures above the obstacle on the cumulated motion [case 1 → 2, Fig. 3(a), center]. (iii) The air channel changes its location in time not only when bypassing the obstacle, but much lower, close to the injection nozzle. On average, therefore, two channels appear both below and above the obstacle [case 2 → 2, Fig. 3(a), right].

The phase diagram (D,h) for the three different dynamics over the whole experimental time is presented in Fig. 3(b). It can be separated into two regions: a stable zone (light blue region), where the air channel does not undergo a large displacement and a single path is observed both below and above the obstacle (case 1 → 1); and an unstable zone, where the air channel alternates its position (above or below) with respect to the obstacle (case 1 → 2 and 2 → 2). The transition between these two regions is found at a height $h \simeq 7.5$ cm for an obstacle diameter $D = 4$ cm. For small obstacles ($D < 2$ cm), the transition appears at $h \simeq 10$ cm, above which the channel is not stabilized anymore by the obstacle but randomly bypasses it on either side. Indeed, for $h \lesssim 10$ cm, the obstacle blocks part of the grain convection that happens in the fluidized zone, and thus it inhibits the change of direction of the channel. Over that critical height, the obstacle has less effect on the global grain motion in the central region, and the channel can more easily fluctuate and possibly change sides in time. For large obstacles, this limit shifts toward smaller h. A possible explanation is that the channel needs to deviate more from the central nozzle in order to bypass the obstacle. Therefore, although the obstacle's presence tends to stabilize it by inhibiting or reducing the granular convection below, the channel itself may be more unstable, and thus it tends to switch more easily to another path.

Another mechanism that could explain the origin of the transition between the stable and unstable channel behavior is the maximum height reached by the air finger, which develops from the injection nozzle, before it undergoes a fingering-to-fracturing transition at $h \simeq 7$ cm [see, for example, Fig. 1(a)]. This latter transition can induce the alternation of the air channel above the obstacle. In this sense, if the obstacle is located below this height, it will not have any influence on the generation of new channels. On the contrary, if it is near or above this height, then the system will be affected by the fingering-to-fracturing transition, and hence it will randomly modify the direction of the air channel.

C. Wake size

Figure 4 displays the wake area $\mathcal{W}$ normalized by the obstacle cross section, eD, as a function of the obstacle height for the different obstacle size and shape. $\mathcal{W}$ is computed according to the image processing presented in Sec. III A. The formation of a significant wake is observed for large obstacles only ($D = 4$ cm). For circular obstacles, the wake size decreases linearly as a function of the obstacle height. Experiments with square or diamond obstacles show a drastic increase of the wake size for these latter geometries—more than twice the wake for the circular obstacles. Although the value of the wake area can be affected by the choice of the threshold in the computation (Sec. III A), this tendency remains, and it can be interpreted as follows. (i) The large obstacles affect more the central air channel rise when they are located close to the injection nozzle, and, as a consequence,

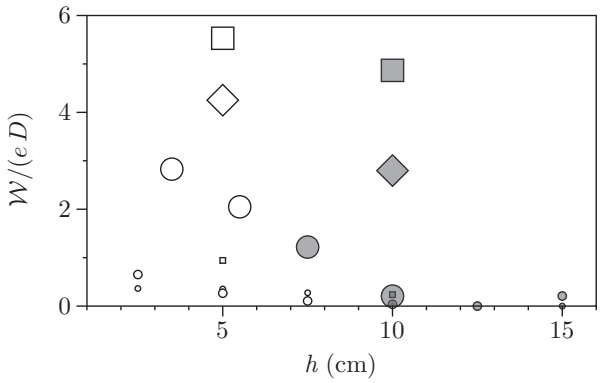

FIG. 4. Normalized wake area $\mathcal{W}/(eD)$ as a function of the obstacle height h. [The symbols in Figs. 4, 5, and 6 are representative of the obstacle shape and size, (symbol, regime): (white, stable); (gray, unstable)].

the wake size is larger for small h. (ii) A square obstacle shape—and, in a more general way, the presence of angles (e.g., diamond shape)—tends to block the streamlines of the grains motion in the fluidized zone. As its equivalent in fluid dynamics, the wake is therefore much larger than in the case of circular obstacles.

D. Air channel deviation

In this section, we quantify the deviation of the air channel induced by the obstacle, both below (Δ_{down}) and above (Δ_{up}) the obstacle [Fig. 3(a), left]. The location of the air channel is computed from the cumulated motion (see Fig. 2), and in the case of two channels above and/or below the obstacle, only the channel with the largest motion is taken into account. Figure 5(a) displays the distance between the vertical of the injection nozzle and the air channel above the obstacle, Δ_{up}. As expected, the larger the obstacle size D, the larger is the air channel deviation above the obstacle. No dependence is found either on the obstacle height or shape. As described in the previous sections, the channel below the obstacle can also exhibit a deviation from the vertical of the injection nozzle. Figure 5(b) displays this shift, Δ_{down}, for the different obstacles' height, size, and shape. For the smaller obstacles ($D \leqslant 2$ cm), the deviation below the obstacle is small, typically about 0.5 cm, and it is roughly independent of the obstacle height and shape. No drastic difference is observed for the large obstacles ($D \geqslant 4$ cm), as in the case of the deviation above the obstacle. For large circular obstacles Δ_{down} decreases with h, and for $h \geqslant 7.5$ cm it reaches the same value as the smaller obstacles. The largest shift below the obstacle is observed for the large square obstacles ($D = 4$ cm), and it also decreases when h increases. For the specific point of the circular obstacle, $D = 1.5$ cm, $h = 15$ cm, and $\Delta_{\text{down}} \simeq 0$. Indeed, in this case, the channel below the obstacle moves a lot and, on average, the program detects no deviation, while in the movies, a clear deviation appears intermittently. This point will be ignored hereafter.

Figure 5(c) displays the air channel deviation due to the obstacle ($\Delta_{\text{up}} - \Delta_{\text{down}}$) normalized by the typical obstacle radius, $D/2$. For all the experiments, $(\Delta_{\text{up}} - \Delta_{\text{down}})/(D/2) < 1$ (below the gray zone). This result indicates that there is always

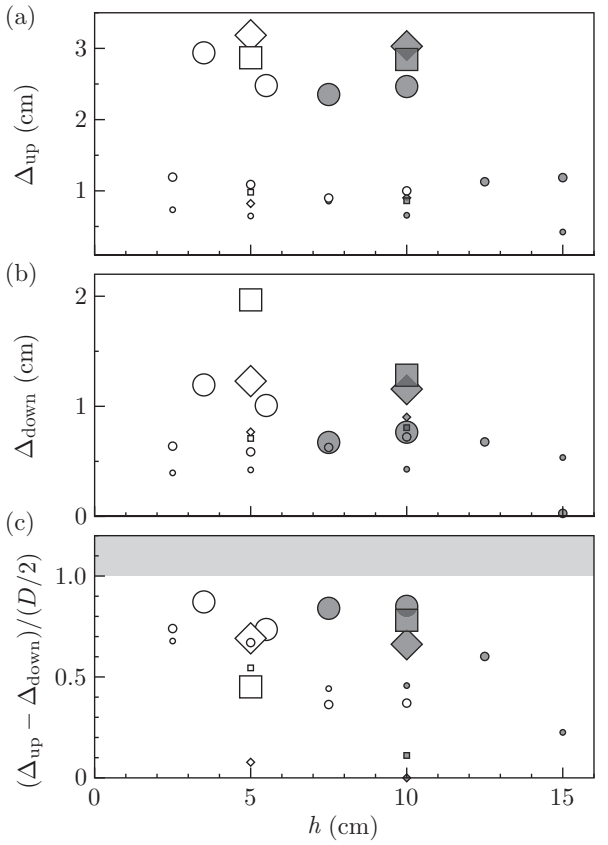

FIG. 5. Distance between the maximum of the air channel (from the cumulated image, see Fig. 2) and the vertical of the injection nozzle (a) above, Δ_{up} and (b) below, Δ_{down} the obstacle. (c) Main deviation of the air channel due to the obstacle ($\Delta_{\text{up}} - \Delta_{\text{down}}$) normalized by the obstacle radius, $D/2$. The gray zone indicates a deviation larger than the typical obstacle radius [(symbol, regime): (white, stable); (gray, unstable)].

a feedback of the channel position above on its position below the obstacle. If the channel bypasses the obstacle on one side, it also shifts position below the obstacle toward this same side, as can be clearly seen in Fig. 2(b) for the large diamond obstacle, for instance.

E. Maximum gas concentration

In this last section, we estimate the location of the maximum gas concentration in the fluidized bed (x_{max},h_{max}), or, in other words, the maximum probability for the presence of bubbles. It corresponds to either (i) the location of the maximum probability of the presence of the central gas channel, due to its repetitive pathways, or (ii) the presence of a gas bubble trapped for a long time in the fluidized bed. To do so, we simply consider the maximum of the cumulated image C (Sec. III B), which gives the highest probability of gas presence in the system [see, for instance, Fig. 1(d)].

Except for the higher large square obstacle [$D = 4$ cm, $h = 10$ cm, gray square in Fig. 6(a)], for which we observed a bubble trapped right below the obstacle, there is a clear separation in the absolute value of the horizontal position $|x_{\text{max}}|$ of the maximum bubble presence between the small ($D \leqslant 1.5$ cm) and the large ($D \geqslant 4$ cm) obstacles. In all cases, $|x_{\text{max}}|$

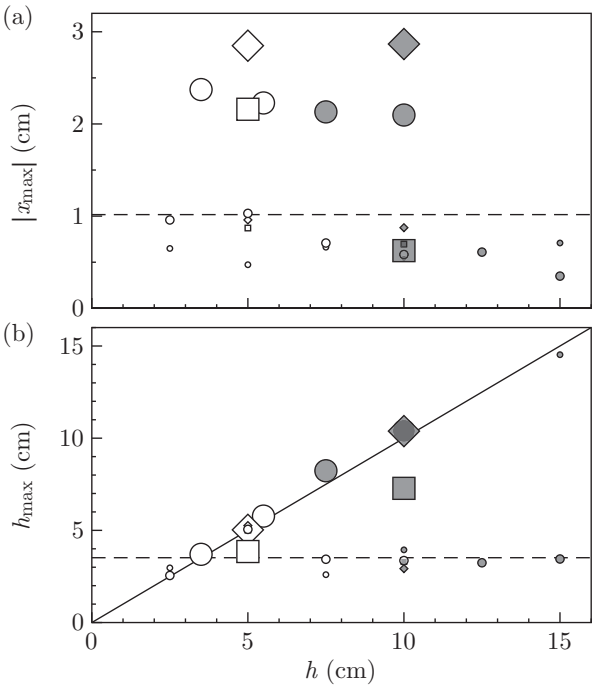

FIG. 6. Location of the maximum probability (x_{max},h_{max}) for the presence of bubbles, computed from the cumulated image C (Sec. III B), as a function of the obstacle height h. (a) Absolute value of the horizontal position $|x_{max}|$. The low value for the large square at $h = 10$ cm is due to a bubble trapped right below the obstacle. (b) Vertical position h_{max} [(symbol, regime): (white, stable); (gray, unstable); the solid line is the 1:1 relationship; the dashed line indicates the value without obstacle].

is of the order of, and slightly larger than, $D/2$. The fact that $|x_{max}| \geqslant D/2$ indicates that whichever the obstacle size and height, the maximum probability to find a bubble in the system is outside the central region delimited by the obstacle width D, even in the case of small obstacles ($D \leqslant 1.5$ cm) when this maximum is located below the obstacle. The dashed line in Fig. 6(a) indicates the value of $|x_{max}|$ for the experiment without obstacle. Contrary to what could be expected, $|x_{max}| \neq 0$. Indeed, even without obstacle, the air channel can experience a deviation at the nozzle exit, up to 1 cm [see Fig. 1(a) and the top right picture of Fig. 2 in Ref. [20], for instance]. Therefore, for small obstacles, $|x_{max}|$ is difficult to interpret quantitatively as the contribution to $|x_{max}|$ can come either from the obstacle influence or from the shift at the nozzle exit.

Figure 6(b) displays the height of the maximum probability for bubble location, h_{max}, as a function of the obstacle height. Here again, a clear distinction can be made between the small ($D \leqslant 1.5$ cm) and large ($D \geqslant 4$ cm) obstacles. For small obstacles ($D \leqslant 1.5$ cm), h_{max} is roughly constant and of about 3.5 cm, close to the value without obstacle [dashed line, Fig. 6(b)]. It corresponds to the steady air finger that forms, in most experiments, from the injection nozzle and remains open for long time scales [see Fig. 1(a)]. In this case, the obstacle deviates this finger ($|x_{max}| \neq 0$), but the bubbles' location in the fluidized zone is not drastically affected. For large obstacles ($D \geqslant 4$ cm), a linear trend is observed, $h_{max} \simeq h$, except for the square obstacles. This linear trend can be explained by the fact that large obstacles tend to trap bubbles at their side. For large square obstacles, bubbles are also trapped but preferentially *below* the obstacle, which explains why the squares are below the $h_{max} \simeq h$ trend. Note the particular case of the small circular obstacle ($D = 1$ cm, $h = 15$ cm), which aligns perfectly on this trend. A careful observation of the images revealed a bubble often trapped close to the obstacle, similar to what happens for large obstacles.

V. DISCUSSION AND CONCLUSION

This work reports on the dynamics of gas channels in a dense suspension in the presence of an obstacle. We have shown that the repetitive pathways of the gas define a central zone of roughly parabolic shape, as was already pointed out in the case without obstacle. Depending on the obstacle size, geometry, and position, the central air channel follows different paths. It leads to three different patterns on the cumulated motion, depending on the number of gas pathway signatures below $\rightarrow$ above the obstacle: $1 \rightarrow 1$, $1 \rightarrow 2$, or $2 \rightarrow 2$. These patterns define two regimes: (i) the channel is stabilized by the obstacle ($1 \rightarrow 1$), or (ii) the channel switches position either above or both above and below the obstacle ($1 \rightarrow 2$ or $2 \rightarrow 2$). The formation of a wake above the obstacle follows the intuition, by analogy to fluid flow: it is larger for large obstacles, and almost negligible for smaller ones.

The maximum gas concentration increases linearly with the obstacle height for large obstacles, indicating that bubbles are systematically trapped close to the obstacle. In real soils, the gas will therefore be trapped preferentially close to large heterogeneities. This does not hold true for small obstacles, i.e., typically of the order of or smaller than the width of the central air channel. In this case, the maximum gas concentration location is constant and fixed by the formation of a steady gas finger developing from the injection nozzle.

This steady air finger, clearly visible in most of the experiments [see, for example, Fig. 1(a)] and already reported in the literature [20,24], seems to have a direct impact on the dynamics of the system. Indeed, in the presence of obstacles we observe a change for $h_c \sim 7$ cm, which corresponds to the height at which the gas undergoes a transition between fingering and fracturing. For instance, for $h \gtrsim h_c$, a different behavior is reported between small obstacles (typically of the order of the gas finger width, $w \simeq 1$ cm, or smaller), which do not perturb much the maximum gas concentration height, and obstacles larger than the gas finger width ($D \geqslant 4$ cm), which trap bubbles at their side.

To quantify the transition between channel fingering and fracturing and its role in channel stabilization in the presence of an obstacle, we follow an argument similar to that of Holtzman *et al.* [25]. We introduce a *modified fracturing number*, N_f^*, a dimensionless number that predicts fracturing in the system by comparing the pressure force that drives fracturing, Δf_p, to the resisting frictional force, Δf_f. The pressure force is similar to that in the horizontal system of Holtzman *et al.* [25]. It is the sum of the capillary pressure, γ/d, where $\gamma = 0.07$ N/m is the air-water surface tension, and the viscous pressure drop, $\eta v/d$, where η is the viscosity and v is the finger velocity, leading to $\Delta f_p = \gamma d(1 + \mathrm{Ca})$, where $\mathrm{Ca} = \eta v/\gamma$ is the capillary number. The resisting

force is mainly due to the frictional resistance [25], and in our vertical configuration the confinement is imposed by the weight of the grains and the water column estimated at the bottom of the obstacle, at a height $(h - D/2)$, which is the height to be compared to the fingering-to-fracturing transition of the rising air finger. It therefore leads to $\Delta f_f = \mu \Delta\rho g[h_g - (h - D/2)]d^2$, where $\mu \simeq 0.3$ is the friction coefficient [25,26] and $\Delta\rho = \bar{\rho} - \rho_{\text{air}} \simeq \bar{\rho}$ is the density difference between the grains-water mixture and air. We can therefore write the modified fracturing number as

$$N_f^* = \frac{\gamma(1 + \text{Ca})}{\mu \bar{\rho} g d(h_g - h + D/2)}. \tag{3}$$

To estimate the capillary number, we compute the velocity as $v = Q/(ew)$, where $Q = 1.98$ mL/s is the air injection flow rate, $e = 2$ mm is the cell gap, and $w \simeq 1$ cm is the finger width, leading to $v \simeq 10$ cm/s, which is compatible with the experimental observations. The effective viscosity of the grains and water mixture is estimated by the semiempirical model of Zarraga *et al.* [27], which predicts the viscosity of dense suspensions up to $\phi \simeq 60\%$:

$$\eta = \eta_w \frac{e^{-2.34\phi}}{(1 - \phi/\phi_{\max})^3}, \tag{4}$$

where $\eta_w \simeq 10^{-3}$ Pa s is the water viscosity and $\phi_{\max} = 62\%$ is the poured random packing [27]. Here we consider $\phi \simeq 56\%$ as the packing fraction in the fluidized zone (*very loose random packing*), leading to $\eta \simeq 0.3$ Pa s. The effective density of the grains and water mixture in the fluidized zone is estimated by $\bar{\rho} = \phi\rho_g + (1 - \phi)\rho_w$, with $\rho_g = 2300$ kg/m^3 the grains density and $\rho_w = 1000$ kg/m^3 the water density, leading to $\bar{\rho} \simeq 1730$ kg/m^3.

Figure 7 displays the phase diagram from Fig. 3(b), modified by representing the obstacle diameter D normalized by the air finger width w, D/w, as a function of the modified fracturing number N_f^* [Eq. (3)]. This scaling makes it possible to separate the stable and unstable regions for the central air channel. For $N_f^* > 0.5$, fracturing occurs before the air finger has reached the obstacle, and thus it chooses randomly to pass the obstacle on one side or the other, leading to channel instability in time. For $N_f^* < 0.4$, the central channel still rises as a stable air finger when it reaches the obstacle. It thus chooses one side that is stable in time.

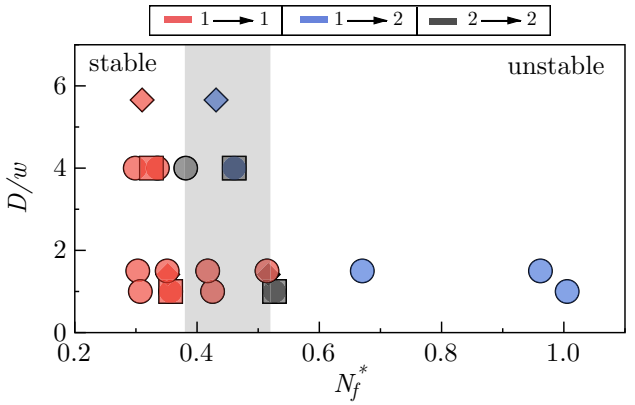

FIG. 7. Normalized phase diagram $(D/w, N_f^*)$, where N_f^* denotes the modified fracturing number describing the transition between fingering and fracturing (see the text). The colors indicate the number of air channels before → after the obstacle, and the symbols represent the obstacle shape. The gray zone displays the transition region, $N_f^* \simeq 0.45 \pm 0.07$.

The width of the transition zone ($N_f^* = 0.45 \pm 0.07$, gray region in Fig. 7) can have different origins. First, the viscosity of the grains-water mixture may vary locally and change the value of the capillary number [Eq. (3)]. Then, the friction coefficient μ has not been measured for our glass beads, and it may be different from the value $\mu = 0.3$; however, it would only shift the transition, and not widen the transition zone. Finally, the grain polydispersity has a direct consequence on the width of the transition zone. Indeed, if we consider the average modified fracturing number at the transition, $N_f^* = 0.45$, to be representative of the average grain size, taking into account the polydispersity $d = 318 \pm 44$ μm leads to $N_f^* = 0.39$–0.52, in agreement with the limits of the transition zone in Fig. 7. We conclude that the transition between fingering and fracturing of the central air channel, and its interaction with the obstacle, is the mechanism controlling the channel stability in time.

ACKNOWLEDGMENTS

G.V. acknowledges financial support from FONDECYT Project No. 11121300 and PUCV DI Regular No. 039.438/2017. This work was supported by Programa de Cooperación Científica ECOS/CONICYT C14E07.

[1] A. R. Dexter, Soil Till. Res. **11**, 199 (1988).
[2] R. Richards Jr., D. G. Elms, and M. Budhu, J. Geotech. Eng. **116**, 740 (1990).
[3] A. Schofield and P. Wroth, *Critical State Soil Mechanics*, European Civil Engineering Series (McGraw-Hill, New York, 1968).
[4] M. Hovland, J. V. Gardner, and A. G. Judd, Geofluids **2**, 127 (2002).
[5] A. Gay, M. Lopez, P. Cochonat, M. Sérane, D. Levaché, and G. Sermondadaz, Mar. Geol. **226**, 25 (2006).
[6] S. Planke, H. Svensen, M. Hovland, D. A. Banks, and B. Jamtveit, Geo-Mar. Lett. **23**, 258 (2003).
[7] V. Mastalerz, G. J. de Lange, A. Dählmann, and T. Feseker, Chem. Geol. **246**, 87 (2007).
[8] A. Mazzini, H. Svensen, G. G. Akhmanov, G. Aloisi, S. Planke, A. Malthe-Sørenssen, and B. Istadi, Earth Planet. Sci. Lett. **261**, 375 (2007).
[9] R. Semer, J. A. Adams, and K. R. Reddy, Geotech. Geol. Eng. **16**, 59 (1998).
[10] K. R. Reddy, R. Semer, and J. A. Adams, Environ. Manage. Health **10**, 52 (1999).
[11] J. S. Selker, M. Niemet, N. G. McDuffie, S. M. Gorelick, and J.-Y. Parlange, Transp. Porous Med. **68**, 107 (2007).

[12] G. Biardi and G. Baldi, Catal. Today **52**, 223 (1999).
[13] K. Pangarkar, T. J. Schildhauer, J. Ruud van Ommen, J. Nijenhuis, F. Kapteijn, and J. A. Moulijn, Ind. Eng. Chem. Res. **47**, 3720 (2008).
[14] W. Ji, A. Dahmani, D. P. Ahlfeld, J. D. Lin, and E. Hill, Ground Water Monit. Rem. **13**, 115 (1993).
[15] K. R. Reddy, S. Kosgi, and J. Zhou, Hazard. Waste Hazard. Mater. **12**, 97 (1995).
[16] X.-Z. Kong, W. Kinzelbach, and F. Stauffer, Chem. Eng. Sci. **64**, 1528 (2009).
[17] G. Ramos, G. Varas, J.-C. Géminard, and V. Vidal, Phys. Rev. E **92**, 062210 (2015).
[18] G. Varas, V. Vidal, and J.-C. Géminard, Phys. Rev. E **83**, 011302 (2011).
[19] G. Varas, J.-C. Géminard, and V. Vidal, Gran. Matter **15**, 801 (2013).
[20] G. Varas, G. Ramos, J.-C. Géminard, and V. Vidal, Front. Phys. **3**, 44 (2015).
[21] R. Poryles, V. Vidal, and G. Varas, Phys. Rev. E **93**, 032904 (2016).
[22] Y. Amarouchène, J. F. Boudet, and H. Kellay, Phys. Rev. Lett. **86**, 4286 (2001).
[23] H. Teufelsbauer, Y. Wang, M.-C. Chiou, and W. Wu, Gran. Matter **11**, 209 (2009).
[24] V. De Zotti and V. Vidal, in *Compte-rendus de la* 17^e *Rencontre du Non-Linéaire*, edited by E. Falcon, M. Lefranc, F. Pétrélis, and C. T. Pham (Non-Linéaire, Paris, 2014), pp. 29–34.
[25] R. Holtzman, M. L. Szulczewski, and R. Juanes, Phys. Rev. Lett. **108**, 264504 (2012).
[26] T. Divoux and J.-C. Géminard, Phys. Rev. Lett. **99**, 258301 (2007).
[27] I. E. Zarraga, D. A. Hill, and D. T. Leighton, J. Rheol. **44**, 185 (2000).